A Collision Efficiency Model for Flow-Induced Coagulation of Fractal Aggregates

Matthäus U. Bäbler
Dept. of Chemistry and Applied Biosciences, Institute for Chemical and Bioengineering, ETH Zurich, 8093 Zurich, Switzerland

DOI 10.1002/aic.11496
Published online April 18, 2008 in Wiley InterScience (www.interscience.wiley.com).

A model for flow-induced collisions of fractal aggregates is developed. The model is based on the analysis of the relative trajectories between a pair of aggregates that takes into account their hydrodynamic and their colloidal interactions. Regarding the former, the aggregates are modeled as permeable spheres where the Brinkman equation is used to describe the flow inside the aggregates. Interparticle forces are incorporated by considering the forces between the primary particles in the two aggregates that are the nearest. The model results in a collision efficiency that depends on the masses of the colliding aggregates, the fractal dimension, and a nondimensional Hamaker constant characterizing the interparticle forces. The collision efficiency model is used to investigate the dynamics of a suspension undergoing coagulation. Significant deviations with respect to existing collision efficiency models are evidenced.
 AIChE J, 54: 1748–1760, 2008
Keywords: colloidal aggregation, relative trajectories, hydrodynamic interaction, permeability, population balance equations

Introduction

The removal of fine particles from a liquid suspension by means of coagulation (aggregation, flocculation) is a common unit operation in the polymer industry and in waste water treatment. In the former, the particles are in the form of a latex, typically produced by emulsion polymerization, with particle sizes in the range of a few tens to hundreds of nanometers. To effectively remove these particles from the suspension the latex is coagulated which results in aggregates (clusters, flocs) with sizes ranging from a few micrometers up to millimeters. Very often, coagulation is thereby performed in an agitated device, e.g., a stirred tank, which enhances the growth rate of aggregates as well as the mixing of coagulation agents. The growth rate of aggregates in a flow, that is to say, the aggregation kinetics in a flow, that becomes the dominant growth mechanism when the aggregates had grown larger than ~ 1 μm is the subject of this article.

In the case where the flow is a simple shear flow and in the absence of any interaction between the particles except sticking upon contact, the collision rate between particles of species i and j reads as $K_{ij}N_iN_j$, where[1,2]

$$K_{ij} = 4/3G(R_{c,i} + R_{c,j})^3, \tag{1}$$

is the collision frequency function, N_i is the concentration of particles i, G is the characteristic velocity gradient (shear rate) of the fluid flow, and $R_{c,i}$ is the collision radius of particle i, i.e., the characteristic radius of particle i that is accessible to collisions. It is recognized that interactions between the particles are negligible only when the particles are vanishingly tenuous, i.e., aggregates with a very open structure,

This article contains supplementary material available via the Internet at http://www.interscience.wiley.com/jpages/0001-1541/suppmat.

Correspondence concerning this article should be addressed to M. U. Bäbler at this current address: Institute of Process Engineering, ETH Zurich, 8092 Zurich, Switzerland; e-mail: baebler@ipe.mavt.ethz.ch.

such that the fluid flow can penetrate the aggregates nearly undisturbed and that interparticle forces acting between the aggregates are negligible. Dense aggregates and solid particles, on the other hand, are subject to strong hydrodynamic interactions when approaching each other[3,4] which significantly influences the collision rate.

The aim of this work is to develop an efficiency factor to the collision rate given earlier, which takes into account the hydrodynamic interactions and the interparticle forces acting between aggregates. This is achieved through the analysis of the relative trajectory between a pair of aggregates. This method was applied in earlier studies[5–9] to investigate the collisions between solid particles. With respect to these studies which are restricted to collisions of impermeable particles (i.e., primary particles) in this work the porous structure of the aggregates is explicitly taken into account.

The collision efficiency of porous aggregates was the subject of earlier studies: Kusters et al.[10] proposed a so-called core-shell model to describe the hydrodynamic interactions of porous aggregates where the aggregates are assumed to consist of an impermeable core surrounded by a completely permeable shell. Ducoste[11] adopted this notion and proposed a semiempirical closed form expression for the collision efficiency that takes into account the interparticle forces acting between the aggregates. Thill et al.[12] used the collision efficiency scheme proposed by Veerapaneni and Wiesner[13] which substitutes the radius in Eq. 1 through an effective collision radius that depends on the aggregate permeability. It is recognized that all these models rely on strong ad-hoc assumptions regarding both the hydrodynamic interaction and the interparticle forces. Moreover, in all these models the aggregate permeability is computed from the aggregate solid volume fraction which leads to very small permeabilities for the aggregates (i.e., large shielding ratios, cf. Eq. 9) which are not in agreement with the settling behavior of porous aggregates.[14] Based on these observations, we see a clear need for a better and more detailed understanding of the collisions between aggregates in order to describe flow-induced coagulation.

Before turning to the collision model, let us consider the structure of the aggregates. It is generally accepted that aggregates formed by Brownian aggregation are fractal objects.[15] This implies that, on average, the number of primary particles in an aggregate, i (hereafter referred to as the mass of an aggregate), scales with its radius R according to $i \sim R^{df}$, where d_f is a fractal dimension. Although less conclusive, the concept of fractal aggregates reveals to very practical for aggregates whose formation is dominated by the flow. Hence, in this work, the fractal scaling is applied in the common form

$$i = k_g(R_g/R_p)^{d_f}, \quad i > 3, \tag{2}$$

where R_g is the radius of gyration of the aggregate, R_p is the radius of the primary particles forming the aggregate, and k_g is a constant which is taken as unity.[16] According to Lattuada et al.,[16] the scaling relation, Eq. 2, is considered to hold for aggregates consisting of more than three monomers.

In the next section, a collision model is introduced which allows us to compute the collision efficiency as a function of the structure of the aggregates. The aggregate structure which determines the hydrodynamic interaction and the interparticle forces is thereby modeled through an effective permeability. A relation between the effective aggregate permeability and the fractal dimension is developed in a subsequent section which enables us to formulate the collision efficiency as a function of the fractal dimension. Results show the obtained collision efficiency and explore its impact on coagulation kinetics. A detailed parameterization of the numerically computed collision efficiency is given in the Supplementary material.

Aggregate Collision Model

The aggregate collision model developed in this article builds on the work of Bäbler et al.[3] (hereafter referred to as BSMB). In BSMB, the porous fractal aggregates were modeled as permeable particles where the Brinkman equation[17] was adopted to describe the flow inside the aggregates. The collision frequency was then determined through the analysis of the relative trajectories between a pair of aggregates. The governing equation thereby is the relative velocity between two approaching aggregates which was derived in a clearly defined framework within BSMB. In particular, it was assumed that the suspension is sufficiently diluted such that only two body interactions occur and that the macroscopic properties of the flow are not altered because of the presence of the particles. Further, the particle Reynolds number $Re = R^2G/\nu \ll 1$ and the particle Stokes number $St = t_pG \ll 1$, where[18] $t_p = R^2(2\rho_s/\rho_f + 1)/(9\nu)$ is the particle relaxation time, i.e., the time taken by the particle to adjust its velocity to the velocity of the surrounding fluid flow. Regarding an aqueous turbulent flow where (at least) $\rho_s/\rho_f < 4$, these conditions are equivalent to the condition that the particles are smaller than the Kolmogorov length scale of the turbulent flow, $\eta = (\nu^3/\varepsilon)^{1/4}$. Additionally, it was assumed that the particle Péclet number $Pe = GR^2/D \gg 1$ such that particle displacement by Brownian diffusion is negligible. Considering an aqueous flow with $G = 100 - 1000\ s^{-1}$, which are typical values found in the coagulation of lattices, BSMB, and hence the present model, refer roughly to particles and aggregates in the size range between 0.1 μm and 30–100 μm.

A scheme of the hydrodynamic problem of the collision between two aggregates is shown in Figure 1a (see figure caption for details). BSMB derived an analytical approximation for the relative velocity through a method of reflections. The relative velocity was presented as a superposition of the relative velocity induced by the fluid flow, $\mathbf{v}^{(flow)}$, and the relative velocity induced by interparticle forces, $\mathbf{v}^{(int)}$, where expressions for the two velocities are given by Eqs. 3 and 4 in BSMB, respectively. With respect to BSMB, the main difference of the present model is the characteristic length scale that determines the interparticle forces, i.e., $\mathbf{v}^{(int)}$. In BSMB, where the aggregate structure was not considered, this length scale was taken as the aggregate size, whereas in the present model, the length scale of the interparticle forces is taken as the primary particle size, as motivated as follows.

The relative velocity induced by interparticle forces depends on the interparticle potential between the aggregates. For fully destabilized particles the interparticle potential is

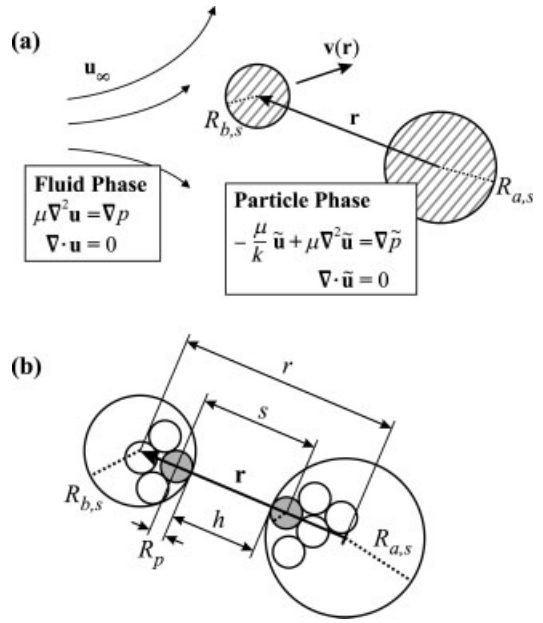

Figure 1. (a) Scheme of the colliding aggregates; (b) interparticle forces of the van der Waals type act between the two primary particles in the aggregates that are the nearest.

For (a) the flow in the vicinity of the aggregates and inside the aggregates is described by the quasi steady creeping flow equation and by the Brinkman equation, respectively. In both flow domains, the flow is incompressible. Boundary condition includes the linearity of the flow at infinity and continuity of the velocity and the viscous stress across the particle surface.

governed by attractive forces of the van der Waals type. These forces act on relatively short distances with respect to the aggregate size. Regarding two approaching aggregates, because of the rapid decay of the interparticle forces with increasing separation distance, we have that only the interparticle forces acting between the two primary particles that are the nearest contribute significantly to the interparticle force acting between the aggregates.[10] This is illustrated in Figure 1b, where $R_{a,s}$ is the radius of the smallest sphere encompassing the aggregate. Hence, the interparticle potential between two aggregates separated by a distance r is taken as the van der Waals potential[19] between two primary particles separated by a distance $s = r - (R_{a,s} + R_{b,s}) + 2R_p$ (Figure 1b),

$$\psi = -\frac{A_H}{6}\left[\frac{2R_p^2}{s^2 - 4R_p^2} + \frac{2R_p^2}{s^2} + \ln\left(\frac{s^2 - 4R_p^2}{s^2}\right)\right], \qquad (3)$$

where A_H is the Hamaker constant which for hydrocarbons in an aqueous solution assumes $A_H \approx 3 \times 10^{-21}$ J. For large primary particles (>0.1 μm) retardation effects become significant,[19] which lead to a reduction of the interparticle potential given by Eq. 3. Schenkel and Kitchener[20] provide the following empirical expression to account for retardation[3]:

$$\psi = -\frac{A_H}{6}\frac{R_p}{h}f(p);$$

$$f(p) = \begin{cases} (1 + 1.77p)^{-1}, & p \le 0.5709 \\ 0.49p^{-1} - 0.1447p^{-2} + 0.01686p^{-3}, & p > 0.5709 \end{cases} \qquad (4)$$

where h is the surface-to-surface distance between the particles, and $p = 2\pi h/(N_L R_p)$. Thereby, the retardation parameter reads as

$$N_L = \lambda_L / R_p \qquad (5)$$

where λ_L is the London wave length that assumes typically $\lambda \approx 100$ nm. It is noticed, however, that for large N_L, i.e., small primary particles, Eq. 4 does not reduce to Eq. 3, and in the limit $N_L \to \infty$ it even predicts stronger interactions than Eq. 3 which is not feasible. Hence, in the present model the nonretarded potential (Eq. 3) is chosen whenever the retarded potential (Eq. 4) leads to a larger collision efficiency.

When the two approaching aggregates are very close, surface asperities of the primary particles start to influence the interaction and the overlapping electron clouds of the particles lead to a Born repulsion acting to exclude the particle volumes. This additional interaction is simply modeled as an infinite repulsion force acting when the surface-to-surface distance between the aggregates is smaller than a critical value denoted by h_{min}. With this force taken into account, the interaction potential has a deep minimum at $s = h_{min} + 2R_p$. Aggregates entrapped in this minimum are regarded to be aggregated. Typical values of h_{min} for polymeric lattices are of the order of a few angstroms to a few nanometers depending on the surface structure. To keep the number of parameters reasonable, in this work we set $h_{min}/R_p = 0.01$.

The relative velocity induced by the fluid flow, $\mathbf{v}^{(flow)}$, depends on the undisturbed flow on the length scale of the particles (that is, the flow in the absence of the particles). In the present model, the undisturbed flow is assumed to be a linear axisymmetric extensional flow of magnitude E, i.e., $\mathbf{u}_\infty = E(-\frac{1}{2}x_1, -\frac{1}{2}x_2, x_3)^T$. An illustration of the particle trajectories in this flow is given in Figure 4 in BSMB. Regarding coagulation in a turbulent flow, the axisymmetric extensional flow was adopted in several studies[21–23] to represent an effective flow field responsible for flow-induced collisions of neutrally buoyant particles below the Kolmogorov length scale. This holds on Batchelor's[24] investigation of mass transfer from the surface of a small sphere in a turbulent flow. In this work, the component of the flow field responsible for mass transfer to the particle surface was identified as a pure straining motion axisymmetric about the vorticity vector. From the analysis of the velocity correlation functions in isotropic homogeneous turbulence, Batchelor further derived[24]

$$E = \frac{7}{6\sqrt{15}} S \left(\frac{\varepsilon}{\nu}\right)^{1/2}, \qquad (6)$$

where S is the negative skewness factor of the longitudinal velocity derivative which in developed turbulence assumes $S \approx 0.5 - 0.6$.

Having determined the relative velocity, the relative trajectories follow through the integration of the relative velocity and the collision frequency is obtained by identifying the trajectories that lead to collisions. It is convenient to compute the relative trajectories in spherical coordinates (r, θ, ϕ, where r, θ, and ϕ are the radial coordinate, and the polar and the azimuthal angle, respectively. In nondimensional form, the relative velocity then reads as

$$\dot{\rho} = \frac{1}{2}\rho(1-A)(3\cos^2\theta - 1) + \frac{GN_F Y(\rho, N_L)}{18\pi\lambda}\left(\frac{R_p}{R_{a,s}}\right)^2,$$
$$\dot{\theta} = -\frac{3}{2}(1-B)\sin\theta\cos\theta, \tag{7}$$
$$\dot{\phi} = 0,$$

where $\rho = 2r/(R_{a,s} + R_{b,s})$ and $\lambda = R_{b,s}/R_{a,s}$, $(R_{b,s} \leq R_{a,s})$ are the nondimensional separation distance and the particle size ratio, respectively. The first rhs term in the first equation of Eq. 7 describes the change in the separation distance due to the velocity gradient of the fluid flow, while the second rhs term describes the change in the separation distance due to interparticle forces. Accordingly, $Y(\rho)$ is the nondimensional interparticle force, $Y(\rho, N_L) = -(6R_p/A_H) \times (d\varphi/ds)$, and

$$N_F = \frac{A_H}{\mu R_p^3 E}. \tag{8}$$

N_F defined in this form is a measure of the strength of the interparticle forces with respect to the hydrodynamic forces. In the coagulation of polymeric latices, N_F assumes values in the range $(10^{-5}, 10^3)$ (large and small primary particles immersed in intense and weak flow, respectively). Further, A, B, and G in Eq. 7 are hydrodynamic mobility functions[4,26] which for the case where the flow inside the particles is governed by Brinkman equation were derived in BSMB (Eqs. 31, 32, and 40 in BSMB). Finally, dotted variables in Eq. 7 indicate derivatives with respect to a nondimensional time, defined as tE.

Next to the particle sizes $R_{a,s}/R_p$ and $R_{b,s}/R_p = \lambda \times (R_{a,s}/R_p)$ that define the geometry of the encounter, the trajectory equation, Eq. 7, contains four more parameters. These are, on one hand, the nondimensional permeabilities of the two particles, referred to as shielding ratios,[27]

$$\xi_j = R_{j,s}/\sqrt{k_j}, \quad j = a, b, \tag{9}$$

and which enter Eq. 7 through the hydrodynamic functions A, B, and G. On the other hand, there is the nondimensional Hamaker constant, N_F, and the retardation parameter, N_L, which characterizes the interparticle forces. In the next section, we will develop relations to express the former of these quantities, i.e., R_s/R_p and ξ_j, as a function of the fractal dimension and the aggregate mass. Regarding the hydrodynamic functions A, B, and G, in BSMB it was found that they are accurate for shielding rations below $\xi \approx 10$. The error is however still reasonable at a shielding ratio as a large as $\xi \approx 20$ (the error in the collision frequency at $\xi \approx 20$ was estimated to be 14% by comparing approximations of A and B of different order). From the relation for the particle permeability which is presented in the next section, these critical shielding ratios correspond to a fractal dimension of $d_f = 2.74$ and 2.88, respectively (cf. Figure 2). Therefore, below $d_f = 2.88$, which refers to very dense aggregates, the hydrodynamic mobility functions derived in BSMB are considered applicable.

Permeability of Aggregates

In the following section we address the problem of describing the permeability of a fractal aggregate. We start thereby with exploring the connection between the settling rate of an aggregate and its permeability. The settling rate is the most prominent manifestation of aggregate permeability and its exploration will allow us to quantify any permeability model. Let us consider an aggregate of mass i moving uniformly with velocity $\mathbf{v}$ in a flow at rest at infinity. The Reynolds number based on the aggregate size and the aggregate velocity is assumed to be smaller than unity such that the governing equation describing the fluid flow in the vicinity of the aggregate is the quasi steady creeping flow equation (cf. Figure 1a). The boundary conditions read as $\mathbf{u} = 0$ for $r \to \infty$ and $\mathbf{u} = \mathbf{v}$ at the surface of the primary particles forming the aggregate, where r is the distance from the center of mass of the aggregate. It is clear that with increasing aggregate mass the latter of the two boundary conditions rapidly makes the problem very difficult to solve. Rigorous solutions exits for the monomer, the dimer,[26] and trimers of certain geometry.[28] For larger aggregates, approximative methods have to be used, e.g., the method of Kirkwood and Riseman,[29] applied by Wiltzius[30] and Lattuada et al.,[31] or Stokesian dynamics,[32] applied by Kim and Stolzenbach.[33]

An alternative approach is to model the aggregate as a permeable particle where the Brinkman equation (cf. Figure 1a) is adopted to describe the flow inside the aggregate. Assuming a spherical particle with a uniform permeability distribution, this approach results in a correction of the Stokes law for the drag exerted on the moving particle, which reads as

$$\mathbf{F_r} = 6\pi\mu R_s \sigma \mathbf{v}, \tag{10}$$

where $\mathbf{F_r}$ is the drag force and σ is a correction factor that equates to[34]

$$\sigma = \frac{2\xi^2[1 - \tanh(\xi)/\xi]}{2\xi^2 + 3[1 - \tanh(\xi)/\xi]}, \tag{11}$$

where ξ is given by Eq. 9. With increasing shielding ratio, i.e., with decreasing permeability (for an impermeable particle $k = 0$ and accordingly $\xi \to \infty$), σ converges to unity and Eq. 10 reduces to the Stokes law for the drag on an impermeable sphere.

Two quantities can be deduced from Eq. 10. First, the hydrodynamic radius of an aggregate, R_h, is defined as the radius of an impermeable sphere on which acts the same drag as the one acting on a permeable aggregate when moving with uniform velocity $\mathbf{v}$ in a flow at rest at infinity. Using Stokes law to compute the drag on the impermeable sphere, it follows from Eq. 10 that

$$R_h/R_s = \sigma(\xi). \tag{12}$$

Second, the reduced settling velocity, γ, is defined as the ratio between the settling velocity of an aggregate of size R_s and the settling velocity of an impermeable sphere of equal size on which acts the same drag as the one acting on the permeable aggregate. Using Stokes law for the impermeable sphere, it follows as

$$\gamma = \frac{|\mathbf{v}|}{|\mathbf{v}_{imp}|} = \frac{1}{\sigma(\xi)}, \tag{13}$$

where $\mathbf{v}_{imp}$ is the settling velocity of the impermeable sphere.

From the above relation it becomes clear that to measure σ in a settling experiment, the mass of the aggregate has to be known: from the mass, the force acting on the aggregate follows as $\mathbf{F_g} = iV_p(\rho_p - \rho_f)\mathbf{g}$, which balances the drag force. Hence,

$$\mathbf{v}_{imp} = \frac{iV_p(\rho_p - \rho_f)}{6\pi\mu R_s}\mathbf{g} = \frac{2R_s^2(\rho_p - \rho_f)\varphi}{9\mu}\mathbf{g}, \tag{14}$$

where $\varphi = i(R_p/R_s)^3$ is the solid volume fraction of the aggregate. Adopting the fractal concept in the form $i = k_s(R_s/R_p)^{d_f}$, the solid volume fraction reads as

$$\varphi = k_s(R_s/R_p)^{d_f-3}. \tag{15}$$

Provided that the aggregate mass follows the fractal scaling precisely, knowing the fractal dimension (and the prefactor k_s) is therefore in principle equivalent of having the aggregate mass.

A simple approach to compute the permeability and the correction factor σ is to use a model.[10,12] In general, these models read as $k = R_p^2 f(\varphi)$, where $f(\varphi)$ is a function of the aggregate solid volume fraction that depends on the framework within which the model is developed (see Refs. 12 and 33 for a list of models for k). Such an approach in combination with Eq. 15 is used in all collision efficiency models mentioned in the introduction. Li and Logan[14] undertook a detailed evaluation of this approach. In their experiments, the settling velocity and the size of many aggregates were measured simultaneously in a settling column and the aggregate mass was determined subsequently by redispersing the aggregate. Strong disagreement between the measured and the calculated settling velocity was found, which was assigned to the misalignment of the assumption of a homogeneous permeability distribution inside an aggregate.

To overcome this discrepancy of existing permeability models to describe fractal aggregates, we propose an alternative approach. Basically, an empirical relation is developed by simply analyzing experimental and numerical data of the hydrodynamic radius and the settling velocity. The data considered consist of two sets: (1) Lattuada et al.[31] determined the hydrodynamic radius of Monte-Carlo aggregates by using the method of Kirkwood and Riseman.[29] The fractal dimension of the simulated aggregates was 1.85 and 2.05 for diffusion limited and reaction limited cluster aggregation, respectively. (2) Lasso and Weidman[35] ran controlled settling experiments of hexagonal packed aggregates of small mass in silicone oil. The fractal dimension of these aggregates is taken to be equal to 3.0 even for the smallest aggregate investigated, which consists of five primary particles.

A first observation regarding these data is presented in Figure 2, where the solid points show R_h/R_g in the limit of infinite aggregate mass [in the following denoted as $(R_h/R_g)_\infty$] as a function of the fractal dimension. The two points on the left stem from Lattuada et al.,[31] and for an aggregate of infinite mass with $d_f = 3.0$ we have the solid sphere limit $(R_h/R_g)_\infty = \sqrt{5/3}$. It is seen that $(R_h/R_g)_\infty$ increases linearly with d_f,

$$(R_h/R_g)_\infty = -0.109 + 0.466d_f, \tag{16}$$

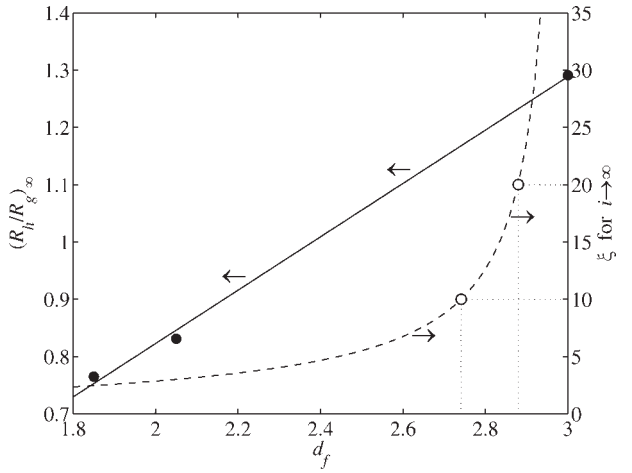

Figure 2. Hydrodynamic radius normalized by the radius of gyration for infinitely large fractal aggregates (solid line), and the corresponding shielding ratio (dashed line) as a function of the fractal dimension.

The solid points refer to numerical data. The open circles refer to a shielding ratio of $\xi = 10$ and 20 corresponding to $d_f = 2.74$ and 2.88, respectively, where the latter represents a critical shielding ratio below which the trajectories are calculated accurately.

shown by the solid line in Figure 2. To compute the correction factor σ and the shielding ratio ξ utilizing Eqs. 11 and 12, the radius of the smallest sphere encompassing the aggregate, R_s, has to be known. In the limit of infinite aggregate mass, R_s is estimated as[36]

$$(R_s/R_g)_\infty = \sqrt{\frac{d_f + 2}{d_f}}. \tag{17}$$

For $d_f = 1.85$ and 2.05, the above estimate gives $(R_s/R_g)_\infty = 1.44$ and 1.41, respectively, which is close to the values found from the Monte-Carlo aggregates[16] which in both cases give $(R_s/R_g)_\infty \approx 1.65$. The dashed line in Figure 2 shows the shielding ratio for $i \to \infty$ as a function of d_f obtained from solving Eqs. 11 and 12 with $(R_h/R_s)_\infty$ from Eqs. 16 and 17. For a fractal dimension $d_f \leq 2.88$, the shielding ratio assumes values $\xi \leq 20$, where $\xi = 20$ is the critical shielding ratio above which the error in the trajectory calculations becomes significant. Note that the drag correction factor for $\xi = 20$ equates to $\sigma = 0.95$, indicating that in a settling experiment such an aggregate is hardly distinguishable from an impermeable particle owning to experimental uncertainty.

Before addressing the shielding ratio for a finite aggregate mass, let us discuss the monomer, the dimer, and the trimer which we refer to as oligomers. These species are assumed to be independent of the fractal dimension and are treated separately in the relation for the permeability. The dimer (for an arbitrary separation of the two monomers) was addressed by Batchelor[26] from which we find $R_h/R_p = 1.39$. For the trimer, the situation is more complicated because the trimer can assume various conformations characterized through the angle ϑ, that is, the angle spanned by the lines connecting

Table 1. Properties of the Oligomers

Oligomer	R_g/R_p	R_h/R_p	R_s/R_p	ξ
Monomer	$\sqrt{3/5}$	1	1	∞
Dimer	$\sqrt{8/5}$	1.39 (Ref. 26)	2	3.94
Trimer*	$\sqrt{2.38-8/9\cos\vartheta}$ (Ref. 41)	1.59 (Ref. 31)	$1+2\sin(\vartheta/2)$	3.07

*Trimer angle $\vartheta = 107^\circ$.

the centers of the primary particles. In this work, we set $\vartheta = 107^\circ$ which is the average angle a trimer assumes if only the geometry of the encounter between a monomer and a dimer is considered. This is close to the value found in Monte-Carlo simulations,[16] where $\vartheta_{av} \approx 103^\circ$. The hydrodynamic radius of the trimer is taken from these simulations as $R_h/R_p = 1.59$. Table 1 summarizes the properties of the oligomers.

Concerning the relaxation of R_h/R_g to its limiting value at infinite mass given by Eq. 16, the two sets of data mentioned earlier can be fitted by

$$(R_h/R_g)_i = (R_h/R_g)_\infty + \left[(R_h/R_g)_3 - (R_h/R_g)_\infty\right]\left(\frac{i+a_1}{3+a_1}\right)^{a_2}, \quad i>3, \quad (18)$$

where $(R_h/R_g)_3 = 0.98$ (Table 1) refers to the triplet and $(R_h/R_g)_\infty$ is given by Eq. 16, and $a_1 = 1.51$ and $a_2 = 9.587 - 7.5d_f + 1.074d_f^2$. Figure 3 shows R_h/R_g as a function of the aggregate mass. The dashed lines refer to the Monte-Carlo aggregates,[31] where $d_f = 1.85$ and $d_f = 2.05$, respectively, and the points refer to the experimental data of Lasso and Weidman,[35] where $d_f = 3$. Considering the whole range of aggregate masses it is observed that for $d_f > 2.34$, R_h/R_g exhibits a minimum at $i = 3$ which is the sharper the larger the fractal dimension. The fact that there must be a minimum for large values of d_f becomes clear when recalling that for a dimer $R_h/R_g < \sqrt{5/3}$, while for a monomer and an infinitely large aggregate with $d_f = 3$ we have $R_h/R_g = \sqrt{5/3}$. The relaxation of the radius of the smallest sphere encompassing the aggregate to its limiting value given by Eq. 17 can be described by the following relation:

$$(R_s/R_p)_i = \sqrt{\frac{d_f+2}{d_f}}(R_g/R_p)_i + \left[(R_s/R_p)_3 - \sqrt{\frac{d_f+2}{d_f}}3^{1/d_f}\right]\left(\frac{i+b_1}{3+b_1}\right)^{b_2}, \quad i>3, \quad (19)$$

where $(R_s/R_p)_3 = 2.61$ (Table 1). The two parameters b_1 and b_2 were chosen according to the two constraints that (1) the limiting value of R_s given by Eq. 17 is reached very rapidly, i.e., at $i \approx 30$ (Ref. 16), and (2) R_s is monotonically increasing with increasing aggregate mass. These constraints are fulfilled by $b_1 = 5$ and $b_2 = -2$.

Summarizing, Eqs. 18 and 19 give the ratio (R_h/R_g) and (R_s/R_p) as a function of the fractal dimension and the aggregate mass from which the correction factor σ and the shielding ratio ξ are computed utilizing Eqs. 11 and 12 (and the fractal scaling relation, Eq. 2). The shielding ratio ξ and the nondimensional aggregate size (R_s/R_p) are the quantities required in the trajectory equation (Eq. 7). Having these quantities as (implicit) functions of d_f and the aggregate mass allows us therefore to formulate the trajectory equation and hence the collision frequency as a function of d_f, the aggregate masses i and j, and the nondimensional Hamaker constant N_F.

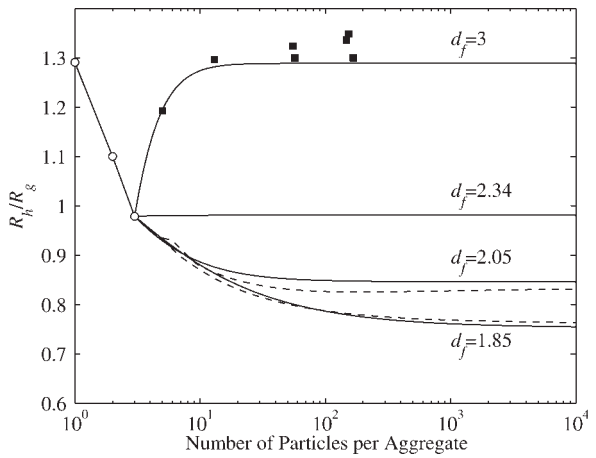

Figure 3. Hydrodynamic radius normalized by the radius of gyration as function of the aggregate mass for various fractal dimensions.

The solid lines refer to Eq. 18, the dashed line shows the results of Lattuada et al.[31] for $d_f = 1.85$ and 2.05, the open circles refer to the oligomers given in Table 1, and the closed squares show the experimental results of Lasso and Weidman[35] taken as $d_f = 3.0$.

Results

Collision efficiency

The model presented in this work results in an expression for the collision frequency function, K_{ij}, as a function of the masses i and j of the colliding aggregates, the fractal dimension, the nondimensional Hamaker constant N_F, and the retardation parameter N_L. It is appropriate to define a collision efficiency, $f_{ij} = K_{ij}/K_{ij}^{(0)}$, by dividing K_{ij} by the geometric collision frequency function $K_{ij}^{(0)}$, that is, the collision frequency function in the absence of any particle interaction. In the given framework, $K_{ij}^{(0)}$ equates analytically to[3]

$$K_{ij}^{(0)} = \frac{4\pi}{\sqrt{27}}E(R_{c,i}+R_{c,j})^3 = k_0 G(R_{c,i}+R_{c,j})^3, \quad (20)$$

where $k_0 \approx 0.36$ follows from Eq. 6 and $G = (\varepsilon/\nu)^{1/2}$. The collision efficiency f_{ij} accounts for the hydrodynamic interaction and the interparticle forces acing between the aggregates. The former causes thereby a deflection of the relative aggregate trajectories which leads to a reduction of the collision ef-

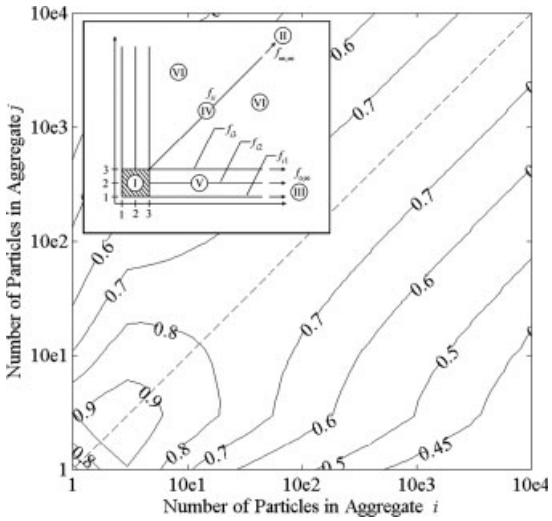

Figure 4. Contour plot of the collision efficiency f_{ij} for $d_f = 2.5$, $N_F = 1$, assuming nonretarded interparticle forces.

The inset shows the scheme for the parameterization of f_{ij}.

ficiency. The attractive interparticle forces, on the other hand, deflect the relative aggregate trajectories oppositely and lead to an increase of the collision efficiency. Hence, the collision efficiency can be either smaller or larger than unity depending on the magnitude of the two types of interactions. Figure 4 shows a contour plot of f_{ij} for $d_f = 2.5$ and $N_F = 1$ assuming nonretarded interparticle forces. It is observed that for these values of d_f and N_F the efficiency steeply increases when increasing the aggregate mass from the monomer to the triplet which is followed by a slow decrease when increasing the aggregate mass further. In addition, the efficiency decreases the more different the two masses are, i.e., when moving away from the diagonal in Figure 4.

Let us explore the behavior of f_{ij} in more detail following the scheme presented in the inset in Figure 4. Region I refers to collisions between oligomers (aggregates with $i \leq 3$) whose structure is assumed to be independent of the fractal dimension. Accordingly, the collision efficiency in this region depends solely on N_F and N_L. Figure 5 shows f_{ij} for $i,j \leq 3$ as a function of N_F. The symbols refer to numerical solutions of the aggregate collision model, and the solid curves present an empirical parameterization of $f_{ij}(d_f, N_F, N_L)$ that is given in the Supplementary material. In all cases, f_{ij} increases with increasing N_F. Note that f_{11}, which refers to the collision between two solid spheres, remains finite even in the limit of vanishing N_F. This result stems from the finite separation at contact which in the present calculations is set to $h_{min}/R_p = 0.01$. In the limit $h_{min} \to 0$ and $N_F \to 0$ the particle remains separated and the collision efficiency drops to zero [this limit is not recovered in the numerical solution of the aggregate collision model where we used analytical approximations to the hydrodynamic functions[3]; however, in a simple shear flow, one must have $h_{min}/R_p < 4.2 \times 10^{-5}$ (Ref. 37) in order to have the particles remaining separated which is within the molecular scale when dealing with colloidal particles]. The reduction of f_{ij} due to retardation of the interparticle force is shown for f_{11} for which retardation has the strongest impact. Thereby, open symbols refer to calculations assuming nonretarded interparticle forces, and bar symbols refer to calculations including retardation. It is seen that retardation significantly reduces the collision efficiency and its effect becomes more pronounced the larger the N_F. This is readily understood by the fact that at weak interparticle forces (small N_F) the aggregate collision is controlled by hydrodynamic interactions, and a weak reduction in the interparticle forces has negligible influence.

Figure 5 shows additionally the collisions efficiency for collision between monomers and triplets (dashed curves in Figure 5) stemming from Ducoste's[11] semiempirical extension of Kusters et al.[10] (hereafter referred to as Kusters-Ducoste model, KD, which is elucidated in the Supplementary material). The collision efficiency stemming from KD, $f_{ij}^{(KD)}$, is defined in the same way as f_{ij} above, that is, by dividing the collision frequency by the collision frequency in the absence of any interactions of the aggregates. KD assumes that the undisturbed flow on the length scale of the particles is a simple shear flow of magnitude G. Hence, the collision frequency in the absence of any particle interactions is given by Eq. 20 with k_0 substituted for $k_0' \approx 1.3$. To compare KD with the model developed within this work, the collision efficiency in the former case is therefore weighted by (k_0'/k_0) as indicated in Figure 5. It is found that the two models lead to similar predictions for collisions between monomers but a significant deviation is observed for collisions between larger oligomers.

Regions II and III in Figure 4 inset refer to collisions between equal aggregates and aggregates with a vanishing mass ratio (i.e., $j/i \to 0$) in the limit of infinite mass of the larger aggregate, respectively. For infinitely large aggregates, interparticle forces which act on the length scale of the pri-

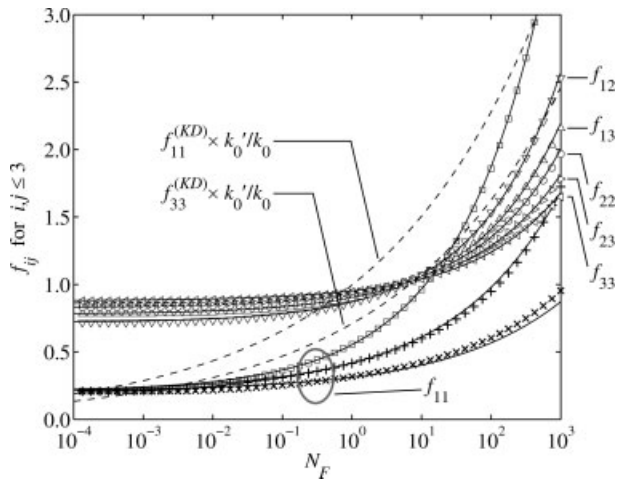

Figure 5. Collision efficiency for the oligomers, i.e., aggregates with mass $i \leq 3$, as a function of the nondimensional Hamaker constant N_F.

The symbols and the solid curves refer to numerical calculations and their parameterization, respectively. Thereby, open symbols refer to nonretarded interparticle forces and bar symbols refer to calculations assuming retarded interparticle forces: (+) $N_L = 10^{-1}$, (×) $N_L = 10^{-2}$. The dashed curves refer to the weighted collision efficiency from the KD model.

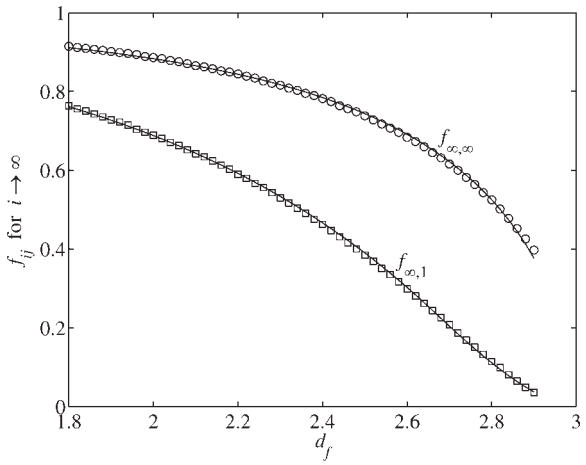

Figure 6. Collision efficiency for aggregates of equal size (○) and aggregates with a vanishing mass ratio (□) in the limit of infinite mass of the larger aggregate as a function of the fractal dimension.

The symbols and the solid curves refer to numerical calculations and their parameterization, respectively.

mary particles become negligible on the length scale of the aggregates. Therefore, f_{ij} in the limit $i \to \infty$ is independent of N_F (and N_L) and is solely governed by the structure of the aggregates characterized through the fractal dimension. Figure 6 shows f_{ii} and f_{ij} for $i \to \infty$ and $j/i \to 0$ as a function of d_f. The symbols refer to the numerical solution of the aggregate collision model and the curves present the empirical parameterization given in the Supplementary material. It is seen that in the considered range of values of d_f the collision efficiency between equal aggregates is always larger than the collision efficiency between unequal aggregates. Regarding the latter, we note that modeling the colliding aggregates as permeable spheres of size R_s becomes a strong assumption for $j/i \to 0$: If the two colliding aggregates are very open and differ substantially in size it might occur that the smaller aggregate penetrates the sphere describing the larger aggregate without undergoing any physical contact to the larger aggregate, and we have that the encounter becomes unsuccessful. Such a case is not included in the aggregate collision model and $f_{\infty,1}$ shown in Figure 6 presents therefore an upper limit of the collision efficiency for collisions with $j/i \to 0$. In the coagulation of a particle population it occurs, however, that these collisions are less frequent simply due to the geometry of the encounter (cf. Eq. 20) and it is found that they are less important for the evolution of a particle population undergoing coagulation. (In the simulation of coagulation presented below, the effect of penetrating aggregates is accounted for through the choice of the collision radius in Eq. 20.) Last, from Figure 6 we see that when the fractal dimension approaches $d_f = 3$ infinitely large aggregates become hydrodynamically equivalent to impermeable spheres and the collision efficiency drops to zero. [Note that the numerical calculations with approximated hydrodynamic functions recover the solid sphere limit (i.e., $f_{ij} = 0$) only in the case of a vanishing aggregate mass ratio. The parameterization given in the Supplementary material is, however, constructed such that the limit $f_{ij} = 0$ for $d_f = 3$ and $i \to \infty$ is recovered for $0 \le i/j \le 1$.] Also, we note that KD gives $f_{ij}^{(KD)} = 0$ for $i \to \infty$.

Regions IV and V in Figure 4 inset refer to collisions between equal aggregates of finite mass and collisions between an aggregate of finite mass and an oligomer, respectively. It is clear that with increasing mass of the larger aggregate, regions IV and V approach regions II and III, where, as discussed earlier, the efficiency becomes independent of interparticle forces. On the other hand, with decreasing mass of the larger aggregate, regions IV and V approach region I, where the efficiency becomes independent of the fractal dimension. The relaxation between these two limits is shown in Figure 7, where f_{ii} and $f_{1,i}$ are plotted as a function of the aggregate mass i for four sets of the parameters d_f and N_F (cf. figure caption) assuming nonretarded interparticle forces. Retardation (not shown) is thereby found to lead to a slightly faster relaxation between the two limits (its effect is readily assessed through the parameterization given in the Supplementary material). The efficiency for equal aggregates (Figure 7a) rapidly relaxes to the limiting value where the

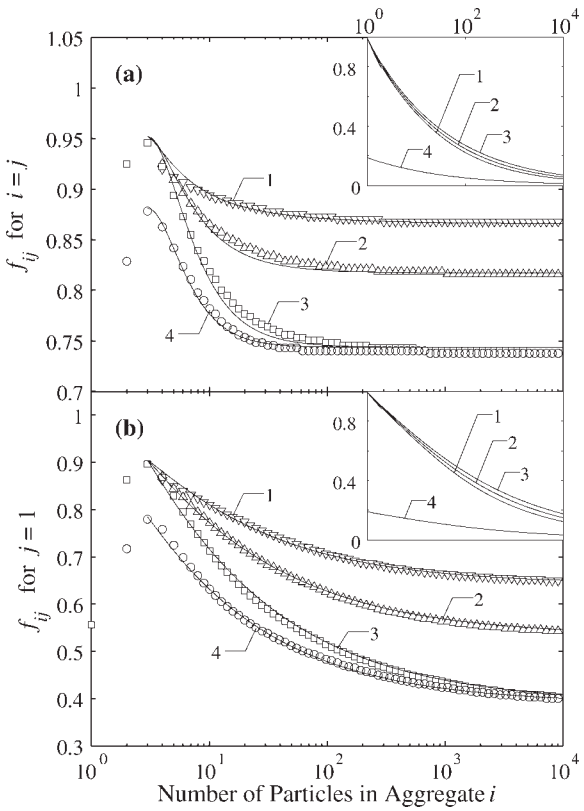

Figure 7. Collision efficiency for (a) aggregates of equal size and (b) an aggregate of mass *i* and a monomer as a function of the aggregate mass *i*.

The symbols and the curves in the main axis show numerical calculations and their parameterization, respectively. The insets show the weighted collision efficiency from the KD model, i.e., $f_{ij}^{(KD)} \times (k_0' / k_0)$. The conditions are (1) $d_f = 2.1$, $N_F = 1$, (2) $d_f = 2.3$, $N_F = 1$, (3) $d_f = 2.5$, $N_F = 1$, and (4) $d_f = 2.5$, $N_F = 10^{-4}$. All curves assume nonretarded interparticle forces.

hydrodynamic interaction, characterized through the fractal dimension, alone controls the collision. Hence, we have that the asymptotic value of f_{ii} decreases with increasing d_f (curves 1–3) and becomes independent of N_F, as seen in the overlapping of curves 3 and 4 for large N_F. The efficiency for the collision of an aggregate of mass i with a monomer (Figure 7b) relaxes substantially slower reflecting the sensitivity of the trajectory of a monomer to the structure of its larger collision partner and to interparticle forces. The collision efficiency stemming from KD is shown in the insets in Figure 7 [where $f_{ij}^{(KD)}$ is weighted by (k_0'/k_0)]. A substantial difference to f_{ij} shown in the main axis is observed. KD predicts a fast decay of the efficiency with increasing aggregate mass, and for the conditions shown in Figure 7, we have $f_{ij}^{(KD)} \times (k_0'/k_0) < 0.2$ at $i = 10^4$. Further, for a given value of N_F, KD predicts a weak increase of $f_{ij}^{(KD)}$ with increasing d_f which is in disagreement with the notion that dense aggregates are subject to stronger hydrodynamic interactions and should therefore obey a smaller collision efficiency. On the other hand, KD predicts a strong dependency on N_F within the whole range of cluster masses which is illustratively seen by the small values assumed by curve 4 which refers to $d_f = 2.5$ and $N_F = 10^{-4}$ whereas curves 1–3 refer to $N_F = 1$.

It remains to address region VI in Figure 4 inset, which refers to collisions between nonequal aggregates of arbitrary mass. Figure 8 shows f_{ij} for a fixed $i = 10^3$ as a function of the mass of the smaller aggregate. It is seen that for a large mass of aggregate i, the collision efficiency relaxes from f_{ii} to f_{3i}, which were discussed in the context of regions IV and V, respectively. For a small mass of aggregate i (not shown), the situation is inverted and f_{ii} is smaller than f_{i3} (cf. parameterization in the Supplementary material). The inset in Figure 8 shows the collision efficiency computed from KD. Apart from the fact that $f_{ij}^{(KD)}$ assumes significantly smaller values than f_{ij} shown in the main axis, we observe an increase in the efficiency with decreasing mass of the smaller aggregate.

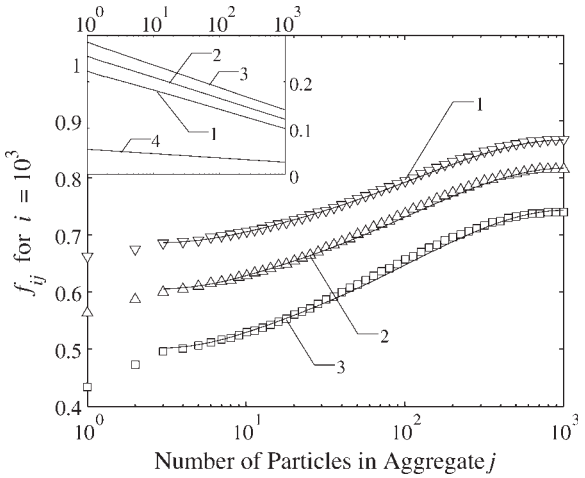

Figure 8. Collision efficiency for nonequal aggregates as a function of the mass of the smaller aggregate.

The mass of the larger aggregate is kept constant at $i = 10^3$. Symbols and curves have the same meaning as in Figure 7.

Evolution of the cluster mass distribution

In the remainder of this section the influence of the collision efficiency on the coagulation dynamics is investigated. For this purpose, let us consider an ensemble of particles suspended in an infinite homogeneous flow which undergoes coagulation. The evolution of the cluster mass distribution (CMD) is governed by a population balance equation which in nondimensional form reads as

$$\frac{dn_i}{d\tau} = \frac{1}{2}\sum_{j=1}^{i-1} \kappa_{j,i-j} n_j n_{i-j} - n_i \sum_{j=1}^{\infty} \kappa_{i,j} n_j \qquad (21)$$

where n_i is the number of particles of mass i normalized by the total number of monomers, $N_{10} = \phi/V_p$, ϕ is the solid volume fraction of the suspension, and κ_{ij} and τ are the nondimensional collision frequency and a nondimensional time, respectively. The first term on the rhs of Eq. 21 accounts for the increase in the number of particles of mass i due to aggregation of two smaller particles, and the second term accounts for the decrease of the number of particles of mass i due to the aggregation with any other particle. To express κ_{ij} as an explicit function of the aggregate masses i and j, we need a relation for the collision radius $R_{c,i}$. In the following we use $R_c \approx R_p i^{1/d_f}$, $i \geq 1$, i.e., the collision radius (for large aggregates) is assumed to be proportional to the radius of gyration. This choice appears more feasible than using the radius of the smallest sphere encompassing the aggregate, $R_{s,i}$: Considering the collision between aggregate i and j, the two spheres of radius $R_{s,i}$ and $R_{s,j}$ may touch in a location where no primary particles are present, and, hence, such a collision would not lead to aggregation. With the given expression for $R_{c,i}$, the nondimensional collision frequency function and the nondimensional time read as $\kappa_{ij} = K_{ij}/(k_0 G R_p^3)$ and $\tau = t \times (k_0 G R_p^3 N_{10})$, respectively. Equation 21 is solved using a fixed pivot discretization scheme[38] with the rate function κ_{ij} evaluated at the position of the pivots. In the present implementation, 480 pivots are used to geometrically discretize the aggregate mass. The geometric spacing between two pivots was thereby chosen as 1.042 which lead to a maximal aggregate mass of $i_{max} = 3.4 \times 10^9$ that is resolved in the calculations [the geometric spacing between the pivots starts at a mass equal to 24; below, the mass is discretized linearly with a spacing of unity providing that the (arithmetic) spacing between neighboring pivots is always greater or equal than unity]. Further details are given elsewhere.[39,40]

Coagulation processes are typically monitored through some integral quantities of the CMD, e.g., an average particle size. Regarding the coagulation of latex particles, a common technique to measure such an integral quantity is light scattering. In the simplest setup, referred to as static light scattering, the intensity of the scattered light is measured as a function of the scattering angle with respect to the incident light beam. This technique provides two integral quantities of the CMD which are the so-called zero angle intensity, I_0, i.e., the intensity of the scattered light extrapolated to a scattering angle of zero, and a mean radius of gyration, $\langle R_g \rangle$. These two quantities are related to the CMD through[39,41]

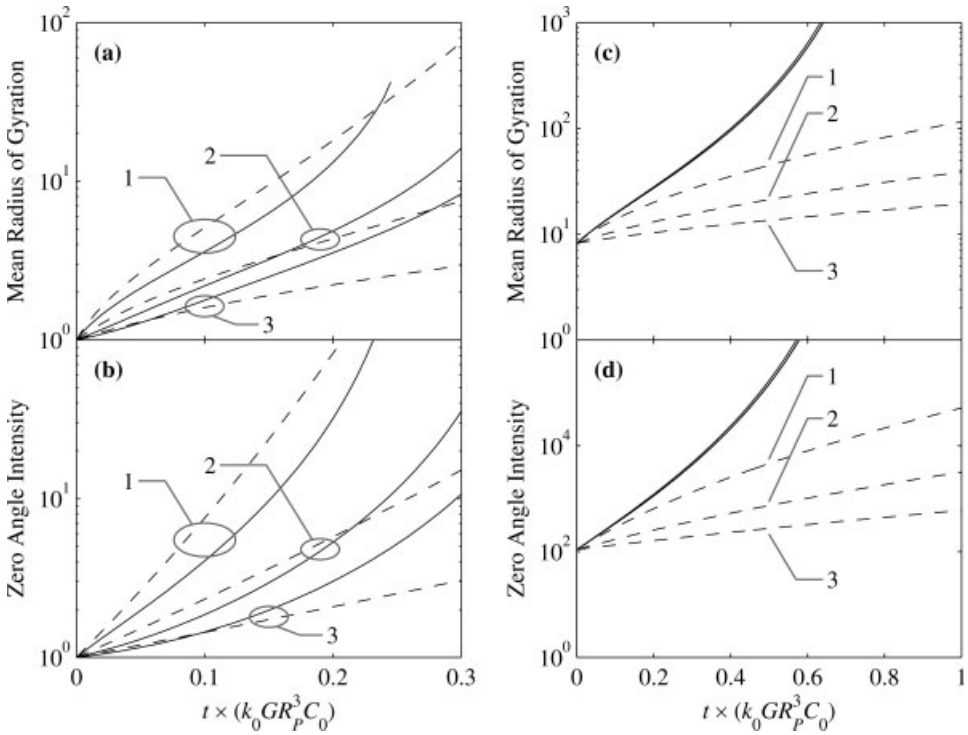

Figure 9. Evolution of the nondimensional mean radius of gyration and zero angle scattering intensity as a function of the nondimensional time for (a, b) a monodisperse initial distribution and (c, d) an initial β-distribution.

The solid and the dashed curves refer to the efficiency model developed within this work and to the KD model, respectively. Curves in the left panels (a, b) have $d_f = 2.1$ and curves in the right panels (c, d) have $d_f = 2.6$. In all panels, curves 1–3 refer to $N_F = 10^{-2}$, 10^0, and 10^2, respectively, and nonretarded interparticle forces are assumed.

$$\langle R_g \rangle = \left(\frac{\sum_{i=1}^{\infty} i^2 n_i R_{g,i}^2}{\sum_{i=1}^{\infty} i^2 n_i} \right)^{1/2}; \quad I_0 = C(\phi) \frac{\sum_{i=1}^{\infty} i^2 n_i}{\sum_{i=1}^{\infty} i\, n_i}, \qquad (22)$$

where $R_{g,i}$ is the radius of gyration of an aggregate of mass i which for $i \leq 3$ is given in Table 1 and by Eq. 2 otherwise, and $C(\phi)$ is a factor depending on the solid volume fraction. Note that $\langle \cdot \rangle$ refers to the mean defined through Eq. 22 and not to an ensemble average. In the following, the mean radius of gyration and the zero angle intensity are reported in nondimensional form, which are obtained by referring to a reference state where the suspension consists only of monomers. Hence, nondimensional quantities are obtained by dividing the above quantities by $\langle R_g \rangle_{ref} = R_{g,1}$ and $I_{0,ref} = C(\phi)$.

Figure 9 shows the time evolution of the two integral quantities given above. In case A (Figure 9a, b), the initial CMD is assumed to consist only of monomers, i.e., the initial condition to Eq. 21 reads as $n_i(t = 0) = \delta_{1i}$. This case describes the initial stage of a typical aggregation experiment. The fractal dimension in such an initial stage is small,[39,42–44] and Figure 9a, b shows calculations assuming $d_f = 2.1$. The solid and the dashed curves refer to the collision efficiency model developed in this work and to KD, respectively, and the enumerated pairs of curves indicate different values of N_F ($N_F = 10^{-2}$, 10^0, 10^2 for curves 1–3, respectively; nonretarded interparticle forces are assumed in all calculations). In case B (Figure 9c, d), the initial CMD is assumed to consist of aggregates with masses in the range $(0,i_0)$ that obey a β-distribution, i.e., the initial condition to Eq. 21 reads as $n_i(t = 0) = Ai^a(i_0 - i)^b$, where $a = 2$, $b = 6$, $i_0 = 300$, and $A \approx \Gamma(a + b + 3)/[\Gamma(a + 2) \rightarrow \Gamma(b + 1)]$ is the normalization factor (determined through $\Sigma_i\, i \times n_i \equiv 1$). The physical scenario described in this case may be found in an aggregation-breakage experiment, where in a first stage of the experiment the aggregates grow until the CMD reaches a steady state where aggregation and breakage balance. The β-distribution given above shall correspond to the steady-state CMD at the end of this first stage where we set accordingly $\tau = 0$. When lowering now the agitation rate, i.e., lowering the shear rate, the aggregates may grow to larger sizes.[45,46] This is referred to as the second stage of our thought experiment, and Figure 9c, d shows the time evolution of $\langle R_g \rangle$ and I_0 in this second stage. The fractal dimension in such a second stage is typically large due to breakage and restructuring having occurred in the first stage.[39,42,46,47] Accordingly, in Figure 9c, d, we have $d_f = 2.6$ and the different curves correspond again to different values of N_F.

In case A (Figure 9a, b), both our model (solid curves) and KD (dashed curves) predict a similar evolution of $\langle R_g \rangle$ and I_0 in the early stage of the process. KD appears to be more sensitive to N_F than our model but the difference is small. At later stages, the two models start to deviate and our model predicts a fast increase of the integral quantities with time while KD predicts roughly an exponential growth. The situation is different in case B (Figure 9c, d), where KD

deviates substantially from our model. For the values of N_F shown, KD predicts a very slow growth of the aggregates, and moreover, the growth rate strongly depends on N_F. Our model, on the other hand, exhibits only a weak dependency on N_F reflecting the fact that collisions of large aggregates are controlled by their hydrodynamic interactions and the interparticle forces (characterized through N_F) play only a minor role. Experiments of the kind underlying case B show that the (re)growth from a steady-state CMD is fast, i.e., comparable to the initial growth rate of the aggregates,[45,46] favoring clearly our model against KD.

Uniform efficiency for the initial aggregate growth

We close this section by discussing the possibility of using a uniform efficiency, $\bar{f}$, for the initial aggregate growth. Figure 10 shows a phase space representation where the zero angle intensity is plotted as a function of the mean radius of gyration. For simplicity, nonretarded interparticle forces are assumed. The solid curves refer to our model, whereas the dashed curves refer to an uniform collision efficiency. Note that in the latter case, the collision efficiency determines solely the time evolution of the CMD, which is evidently absent in the phase space representation shown in Figure 10 (hence, Figure 10 can be drawn without knowing $\bar{f}$). It is observed that for values of N_F around unity, our model (solid curves) predicts a relative evolution of the two integral quantities that is close to the prediction using a uniform efficiency (dashed curves). For smaller (larger) values of N_F, I_0 from our model evolves slower (faster) with respect to the uniform efficiency. Thus, in a limited range of N_F, we can formulate the following empirical expression for the uniform efficiency to compute the initial time evolution of $\langle R_g \rangle$ and I_0:

$$\bar{f} = (1.29 - 0.10 \ \ln N_F)^{-1}, \quad 10^{-2} < N_F < 10^2. \qquad (23)$$

which is obtained by fitting the time evolution computed with our efficiency model. The insets in Figure 10 show the time evolution of $\langle R_g \rangle$ and I_0 computed with our efficiency model (solid curves) and the uniform efficiency given by Eq. 23 (dashed curves). Good agreement is found for $N_F = 1$ (curve 4), whereas the evolution of both $\langle R_g \rangle$ and I_0 are slightly underestimated and overestimated, for $N_F = 10^{-2}$ (curve 3) and $N_F = 10^2$ (curve 5), respectively.

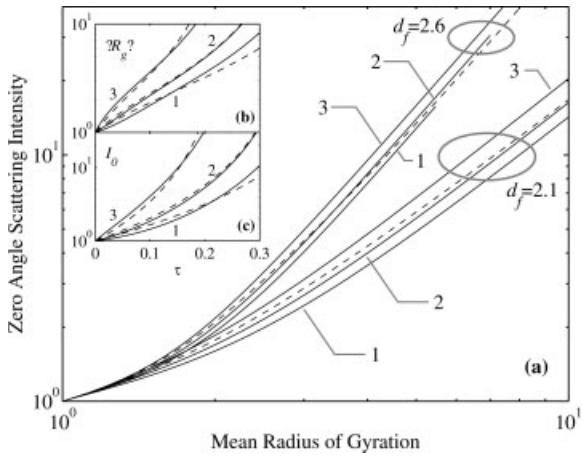

Figure 10. (a) Zero angle scattering intensity vs. the mean radius of gyration; the solid and the dashed curves refer to the collision efficiency model developed within this work and to a uniform efficiency, respectively; the two sets of curves refer to d_f = 2.1 and 2.6; within each set, curves 1–3 refer to N_F = 10^2, 10^0, and 10^2, respectively, where in all calculations nonretarded interparticle forces are assumed; the insets show the evolution of (b) the mean radius of gyration and (c) the zero angle scattering intensity for d_f = 2.1 according to our collision efficiency model (solid lines) and the uniform efficiency given by Eq. 23 (dashed lines).

Curves 1–3 refer to nonretarded interparticle forces with $N_F = 10^{-2}$, 10^0, and 10^2, respectively.

Summary and Conclusions

A detailed model for flow-induced collisions of fractal aggregates has been developed. The model is based on the analysis of the relative trajectories of a pair of aggregates, and it results in an expression for the collision efficiency as a function of the masses of the two colliding aggregates, the fractal dimension, a nondimensional Hamaker constant, N_F, and a retardation parameter, N_L. A detailed parameterization of the collision efficiency as a function of these four parameters is given in the Supplementary material through a set of simple algebraic relations. For small values of N_F, the collision frequency is found to exhibit a maximum for the collision between two trimers, whereas for very large values of N_F, the collision efficiency decreases monotonically with increasing mass of the colliding aggregates. In both cases, collisions between similar aggregates are preferential vs. collisions between aggregates with different masses. Retardation leads to a reduction in the collision efficiency for small aggregates.

The influence of the collision efficiency on the dynamics of a suspension undergoing coagulation is investigated by means of a population balance equation. A significant influence of interparticle forces characterized through N_F is manifested in the case where the initial suspension consists of primary particles. For an initial suspension consisting of aggregates, the aggregate growth is only weakly dependent on N_F and is controlled by the fractal dimension. Interpreting the initial suspension in this case as the CMD resulting from a balance between aggregation and breakage, the model predicts a reasonable fast regrowth (induced, for example, when lowering the agitation rate) of the aggregates.

Acknowledgments

This work was financially supported by the Swiss National Science Foundation (Grant No. 200020-113805/1) and the Foundation Claude et Giuliana. The author thanks Prof. Massimo Morbidelli for the useful discussions and the suggestions. Valuable comments by Amgad S. Moussa are also appreciated.

Notation

A_H = Hamaker constant, J
D = diffusion coefficient, $m^2\ s^{-1}$
d_f = fractal dimension
E = rate of extension, Eq. 6, s^{-1}
f_{ij} = collision efficiency
G = shear rate, s^{-1}
$\mathbf{g}$ = gravitational acceleration, $m^2\ s^{-1}$
h = surface-to-surface distance between aggregates (Figure 1b), m
K_{ij} = collision frequency function, $m^3\ s^{-1}$
k = aggregate permeability, m^2
k_0 = factor in the geometric collision frequency function, Eq. 20
N_H = nondimensional Hamaker constant, Eq. 8
N_i = number concentration of aggregates i, m^{-3}
N_L = nondimensional retardation parameter, Eq. 5
$p, \tilde{p}$ = pressure, and local mean pressure inside an aggregate, Pa
$R_{c,i}$ = collision radius of aggregate i, m
$R_{g,i}$ = radius of gyration of aggregate i, m
$R_{s,i}$ = radius of the smallest sphere encompassing aggregate i, m
R_p = radius of the primary particle, m
$\mathbf{u}, \tilde{\mathbf{u}}$ = fluid velocity, and local mean fluid velocity inside an aggregate, m s^{-1}
$\mathbf{u}_\infty$ = undisturbed fluid velocity, m s^{-1}
V_p = primary particle volume, m^3

Acronyms

BSMB = collision model of Bäbler et al.[3]
CMD = cluster mass distribution,
KD = collision model of Kusters-Ducoste[11]

Greek letters

$\Gamma(z)$ = gamma function
δ_{ij} = Kronecker delta
ε = turbulent energy dissipation rate, $m^2\ s^{-3}$
η = Kolmogorov length scale, m
λ = aggregate size ratio
λ_L = London wave length, m
μ = dynamic viscosity, kg $(m\ s)^{-1}$
ν = kinematic viscosity, $m^2\ s^{-1}$
ζ = shielding ratio, Eq. 9
ρ = nondimensional center-to-center distance
ρ_f = fluid density, kg m^{-3}
ρ_p = primary particle density, kg m^{-3}
ρ_s = aggregate density, kg m^{-3}
ϕ = solid volume fraction of the suspension
φ = aggregate solid volume fraction, Eq. 15
ψ = interparticle potential, J

Literature Cited

1. Smoluchowski M. Versuch einer mathematischen Theorie der Koagulationskinetik kolloider Lösungen. *Z Phys Chem*. 1917;92:129–168.
2. Elimelech M, Gregory J, Jia X, Williams RA. *Particle Deposition and Aggregation—Measurement, Modelling and Simulation*. New York: Butterworth-Heinemann, 1995.
3. Bäbler MU, Sefcik J, Morbidelli M, Bałdyga J. Hydrodynamic interactions and orthokinetic collisions of porous aggregates in the Stokes regime. *Phys Fluids*. 2006;18:013302.
4. Batchelor GK, Green JT. The hydrodynamic interaction of two small freely-moving spheres in a linear flow field. *J Fluid Mech*. 1972;56:375–400.
5. Zeichner GR, Schowalter WR. Use of trajectory analysis to study stability of colloidal dispersions in flow fields. *AIChE J*. 1977;23:243–254.
6. van de Ven TGM, Mason SG. The microrheology of colloidal dispersions. VII. Orthokinetic doublet formation of spheres. *Colloid Polym Sci*. 1977;255:468–479.
7. Han MY, Lawler DF. The (relative) insignificance of G in flocculation. *J Am Water Works Assoc*. 1992;84:79–91.
8. Greene MR, Hammer DA, Olbricht WL. The effect of hydrodynamic flow field on colloidal stability. *J Colloid Interface Sci*. 1994;167:232–246.
9. Vanni M, Baldi G. Coagulation efficiency of colloidal particles. *Adv Colloid Interface Sci*. 2002;97:151–177.
10. Kusters KA, Wijers JG, Thoenes D. Aggregation kinetics of small particles in agitated vessels. *Chem Eng Sci*. 1997;52:107–121.
11. Ducoste J. A two-scale PBM for modeling turbulent flocculation in water treatment processes. *Chem Eng Sci*. 2002;57:2157–2168.
12. Thill A, Moustier S, Aziz J, Wiesner MR, Bottero JY. Flocs restructuring during aggregation: experimental evidence and numerical simulation. *J Colloid Interface Sci*. 2001;243:171–182.
13. Veerapaneni S, Wiesner MR. Hydrodynamics of fractal aggregates with radially varying permeability. *J Colloid Interface Sci*. 1996;177:45–57.
14. Li X, Logan BE. Collision frequencies of fractal aggregates with small particles by differential sedimentation. *Environ Sci Technol*. 1997;31:1229–1236.
15. Lin MY, Lindsay HM, Weitz DA, Ball RC, Klein R, Meakin P. Universality in colloid aggregation. *Nature*. 1989;339:360–362.
16. Lattuada M, Wu H, Morbidelli M. A simple model for the structure of fractal aggregates. *J Colloid Interface Sci*. 2003;268:106–120.
17. Brinkman HC. A calculation of the viscous force exerted by a flowing fluid on a dense swarm of particles. *Appl Sci Res A*. 1947;1:27–34.
18. Hinze JO. *Turbulence*, 2nd ed. New York: McGraw-Hill, 1975.
19. Hunter RJ. *Foundations of Colloid Science*, 2nd ed. Oxford: Oxford University Press, 2001.
20. Schenkel JH, Kitchener JA. A test of the Derjaguin-Verwey-Overbeek theory with a colloidal suspension. *Trans Faraday Soc*. 1960;56:161–173.
21. Melis S, Verduyn M, Storti G, Morbidelli M, Bałdyga J. Effect of fluid motion on the aggregation of small particles subjected to interaction forces. *AIChE J*. 1999;45:1383–1393.
22. Bałdyga J, Jasińska M, Krasiński A, Rożeń A. Effects of fine scale turbulent flow and mixing in agglomerative percipitation. *Chem Eng Technol*. 2004;27:315–323.
23. Wu H, Lodi S, Morbidelli M. Characterization of particle interaction energy through incipient turbulent aggregation. *J Colloid Interface Sci*. 2002;256:304–313.
24. Batchelor GK. Mass transfer from small particles suspended in turbulent fluid. *J Fluid Mech*. 1980;98:609–623.
25. Sreenivasan KR, Antonia RA. The phenomenology of small-scale turbulence. *Annu Rev Fluid Mech*. 1997;29:435–472.
26. Batchelor GK. Brownian diffusion of particles with hydrodynamic interaction. *J Fluid Mech*. 1976;74:1–29.
27. Debye P, Bueche AM. Intrinsic viscosity, diffusion, and sedimentation rate of polymers in solution. *J Chem Phys*. 1948;16:573–579.
28. Kim S. Stokes flow past three spheres: an analytical solution. *Phys Fluids*. 1987;30:2309–2314.
29. Kirkwood JG, Riseman J. The intrinsic viscosities and diffusion constants of flexible macromolecules in solution. *J Chem Phys*. 1948;16:565–573.
30. Wiltzius P. Hydrodynamic behavior of fractal aggregates. *Phys Rev Lett*. 1987;58:710–713.
31. Lattuada M, Wu H, Morbidelli M. Hydrodynamic radius of fractal clusters. *J Colloid Interface Sci*. 2003;268:96–105.
32. Brady JF, Bossis G. Stokesian dynamics. *Ann Rev Fluid Mech*. 1988;20:111–157.
33. Kim AS, Stolzenbach KD. The permeability of synthetic fractal aggregates with realistic three-dimensional structure. *J Colloid Interface Sci*. 2002;253:315–328.
34. Neale G, Epstein N, Nader W. Creeping flow relative to permeable spheres. *Chem Eng Sci*. 1973;28:1865–1874.
35. Lasso IA, Weidman PD. Stokes drag on hollow cylinders and conglomerates. *Phys Fluids*. 1986;29:3921–3933.
36. Rogak SN, Flagan RC. Stokes drag on self-similar clusters of spheres. *J Colloid Interface Sci*. 1990;134:206–218.
37. van de Ven TGM. *Colloidal Hydrodynamics*. London: Academic Press, 1989.
38. Kumar S, Ramkrishna D. On the solution of population balance equations by discretization. I. A fixed pivot technique. *Chem Eng Sci*. 1996;51:1311–1332.

39. Soos M, Sefcik J, Morbidelli M. Investigation of aggregation, breakage and restructuring kinetics of colloidal dispersions in turbulent flows by population balance modeling and static light scattering. *Chem Eng Sci*. 2006;61:2349–2363.
40. Bäbler MU, Morbidelli M. Analysis of the aggregation-fragmentation population balance equation with application to coagulation. *J Colloid Interface Sci*. 2007;316:428–441.
41. Lattuada M, Sandkühler P, Wu H, Sefcik J, Morbidelli M. Aggregation kinetics of polymer colloids in reaction limited regime: experiments and simulations. *Adv Colloid Interface Sci*. 2003;103:33–56.
42. Selomulya C, Bushell G, Amal R, Waite TD. Understanding the role of restructuring in flocculation: the application of a population balance model. *Chem Eng Sci*. 2003;58:327–338.
43. Waldner MH, Sefcik J, Soos M, Morbidelli M. Initial growth kinetics and structure of colloidal aggregates in a turbulent coagulator. *Powder Technol*. 2005;156:226–234.
44. Flesch JC, Spicer PT, Pratsinis SE. Laminar and turbulent shear-induced flocculation of fractal aggregates. *AIChE J*. 1999;42:1114–1124.
45. Spicer PT, Pratsinis SE, Raper J, Amal R, Bushell G, Meeters G. Effect of shear schedule on particle size, density, and structure during flocculation in stirred tanks. *Powder Technol*. 1998;97:26–34.
46. Soos M, Moussa AS, Ehrl L, Sefcik J, Wu H, Morbidelli M. Effect of shear rate on aggregate size and morphology investigated under turbulent conditions in a stirred tank. *J Colloid Interface Sci*. 2008;319:577–589.
47. Moussa AS, Soos M, Sefcik J, Morbidelli M. Effect of solid volume fraction on aggregation and breakage in colloidal suspensions in batch and continuous stirred tanks. *Langmuir*. 2007;23:1664–1673.

Manuscript received Aug. 16, 2007, and revision received Jan. 30, 2008.